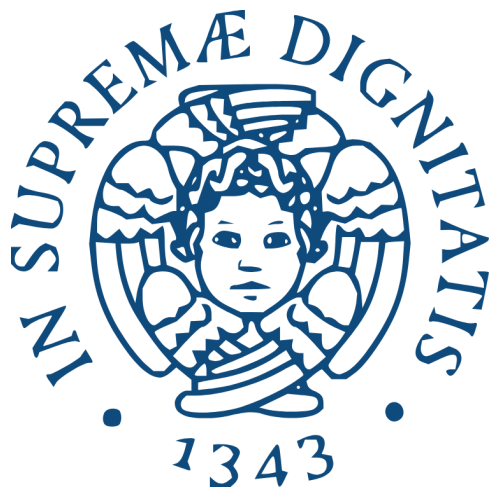


University of Pisa



Laboratory Report

# The Rotation Curve and Spiral Structure of Milky Way from the Hydrogen 21-cm Line Detection with SALSA Radio Telescope

## Professors:

Prof. Massimiliano Razzano  
Prof. Angelo Ricciardone  
Prof. Barbara Patricelli  
Prof. Andrea Pallottini

## Candidates:

Nicolò Aimone Braida (701844)  
Matilde Biscaro (702943)  
Lorenzo Nepi (701845)

## Abstract

The abundance of neutral hydrogen (HI) in the disks of spiral galaxies and its 21 cm emission line due to hyperfine structure transitions make HI one of the fundamental tracers for studying the kinematics of galactic disks. The aim of this experience is to reconstruct the rotation curve of the Milky Way and to map the spiral arm structure of our galaxy based on radio observations of the 21 cm line. Observations were carried out using the 2.3 m SALSA-Onsala radio telescope, covering Galactic longitudes between  $20^\circ$  and  $170^\circ$ . The collected data were analyzed to derive the relative velocities of the HI clouds through the Doppler effect. Subsequently, using considerations on the Galactic geometry, the rotation curve of the Milky Way was traced, revealing the typical plateau at large radii characteristic of spiral galaxies. Finally, based on the results obtained for the rotation curve and assuming differential rotation, a map of the Milky Way was produced, highlighting its spiral structure. The Perseus arm, Orion spur, and Outer arm were identified. During the analysis, the solar rotation speed  $V_0 = 220 \text{ km/s}$  and the distance to the Galactic center  $R_0 = 8.5 \text{ kpc}$  were assumed. The main limitations and sources of error encountered during the experiment are also discussed.

## Contents

<b>1</b>	<b>Introduction</b>	<b>1</b>
<b>2</b>	<b>Theoretical Background</b>	<b>2</b>
2.1	HI in the Milky Way . . . . .	2
2.1.1	The atomic structure . . . . .	2
2.1.2	The HI 21cm . . . . .	2
2.2	Doppler Effect . . . . .	3
2.3	The rotation curve of the Milky Way . . .	3
2.4	Mapping The Milky Way . . . . .	3
<b>3</b>	<b>SALSA Radio Telescope</b>	<b>4</b>
3.1	Limitations . . . . .	5
<b>4</b>	<b>Observation</b>	<b>5</b>
4.1	Telescope settings . . . . .	5
4.2	Measurement results . . . . .	5
<b>5</b>	<b>Data Reduction and Results</b>	<b>6</b>
5.1	Noise subtraction . . . . .	6
5.2	Gaussian fit . . . . .	6
5.3	Rotation curve . . . . .	7
5.4	Map of the Milky Way . . . . .	7
<b>6</b>	<b>Discussion</b>	<b>7</b>
<b>7</b>	<b>Conclusion</b>	<b>7</b>
<b>A</b>	<b>Galactic Coordinates</b>	<b>9</b>
<b>B</b>	<b>Local Standard of Rest</b>	<b>9</b>
<b>C</b>	<b>Keplerian Motion and Dark Matter</b>	<b>9</b>
<b>D</b>	<b>Data reduction results</b>	<b>11</b>
<b>E</b>	<b>Tabulars</b>	<b>13</b>

## References

15

## 1 Introduction

Radio astronomy is a branch of astronomy that studies the universe through the analysis of radio waves emitted by celestial objects. Such observations are possible from the ground because our atmosphere is completely transparent to photons with wavelengths between approximately 1 cm and 15 m (the so-called *radio window*). From the very first observations, it became clear that the radio sky looks very different from the optical one, and that most of the emissions detected in the radio are due to non-thermal processes. This revolutionized our understanding of astrophysics. In particular, radio astronomy allows us to study the interstellar medium and to detect signals that are otherwise obscured by gas and dust in the optical range.

The first radio signal from space was detected in 1933 by Karl Guthe Jansky [10]. In subsequent observations, he noticed that many of the detected signals originated from sources distributed along the galactic plane. In 1945, H.C. van de Hulst predicted the existence of the 21 cm spectral line of neutral hydrogen [2], which was first detected in the Milky Way in 1951 by Ewen and Purcell [8]. That same year, Muller and Oort independently detected the line from Australia [12]. Later, in 1954, the first systematic observation of the 21 cm line was carried out by van de Hulst, Muller, and Oort [9], who surveyed the structure of the Milky Way along the galactic plane using a 7.5 m parabolic antenna with a *beamwidth* of  $1.9^\circ$  in the horizontal direction and  $2.7^\circ$  in the vertical direction. Many other observations were done in the following year, producing a map of the distribution of the neutral hydrogen in our galaxy.

Neutral hydrogen in its ground state is an abundant and widely distributed component of the interstellar medi-

um. Its 21 cm line emission can easily penetrate interstellar dust and gas, making it a powerful tool for studying the structure and kinematics of the Milky Way. The aim of this work is to detect this emission using the SALSA-Onsala 2.3 m radio telescope and to construct both the rotation curve and a spatial map of the Milky Way's spiral arms. We begin by describing the physical mechanism behind HI emission. Then, we present the geometry of the Milky Way, justifying the approximations made to simplify the problem so that the positions of hydrogen clouds can be inferred from observable quantities. We then describe how the observations were carried out and how the data were processed and analyzed, leading to the reconstruction of the dynamics and spatial structure of the Galaxy's spiral arms. We also discuss the uncertainties and limitations of the observations.

## 2 Theoretical Background

This section provides a brief introduction to some concepts and methods that were used to construct the rotation curve and a partial map of the Milky Way starting from the data provided by the SALSA telescope.

### 2.1 HI in the Milky Way

The HI 21 cm line is one of the most important single spectral lines in astronomy because it allows to detect the *Cold Interstellar Medium* and study the structure and dynamics of galaxies. Hyperfine structure transitions in neutral hydrogen cause the emission of photons at 1420 MHz (in the radio band), which can easily penetrate through dust and diffused gas within the galaxy. Among the various reasons that drive astronomers to observe the HI 21 cm line, we should mention the following ones:

- determining the galactic HI mass;
- studying the differential rotation of the Milky Way by mapping HI clouds in the galactic plane;
- determining the kinematics of external galaxies (rotation curves), which allows to compute total masses, study the dark matter halos and use the Tully-Fisher relation for distance determinations.

#### 2.1.1 The atomic structure

The discrete energy-level-structure of an atom and the motion of the electrons is characterized by four quantum numbers: the *principal quantum number*  $n$ , which refers to the quantization of the energy levels, the *orbital quantum number*  $l$ , which is related to the angular momentum of the orbits and their eccentricity, the *magnetic quantum number*  $m$ , which characterizes the component of the angular momentum vector along a preferred direction and the *spin quantum number*, which defines an intrinsic angular momentum of the electrons along a preferred direction. These four quantum numbers characterize single-particle states called *orbitals*.

The full treatment of the energy of the electrons in an atom also requires considering the electrostatic repulsion between the electrons and the spin-orbit interaction. This is addressed using the so-called *LS coupling scheme*,

which evaluates these two additional contributions separately. The *coupling* term describes the method of combining two angular momenta into a resultant one. First, the energy contribution from the electron-electron pair repulsion yields the energy splitting of the configurations into *terms*, which are characterized by the quantities

$$\mathbf{L} = \sum_i \mathbf{l}_i \quad \text{and} \quad \mathbf{S} = \sum_i \mathbf{s}_i, \quad (1)$$

where the sums are vectorial. While calculating the value of  $\mathbf{L}$ , all possible combinations of the  $l$  values for the valence electrons are considered.

Subsequently, the spin-orbit interaction introduces a further splitting into additional energy *levels*, which depends on the sum of the  $\mathbf{l}_i \cdot \mathbf{s}_i$  quantities over all electrons. This splitting arises from the interaction between the magnetic field generated by the orbital motion of the electrons and the total magnetic dipole moment of the electrons. In *LS coupling* scheme the energy contribution from the spin-orbit interaction depends on the total angular momentum vector  $\mathbf{J} = \mathbf{L} + \mathbf{S}$ . The shift in energy between different values of the corresponding quantum number  $J$  is small compared to the energy differences between *terms* and gives rise to the so-called *fine structure* of the energy levels. Transitions between *levels* result in spectral lines, while transitions between terms give rise to *multiplets* (an ensemble of lines).

A fourth contribution arises from the interaction between the total angular momentum of the atom and the *nuclear spin*  $I$ , whose magnitude can have 2 values. This interaction leads to an *hyperfine* splitting, described by the equation  $\mathbf{F} = \mathbf{J} + \mathbf{I}$ , with very small energy differences, in the order of  $10^{-6}$  eV. The Figure 1 summarizes, in a schematic way, the energy splitting due to these different mechanisms.

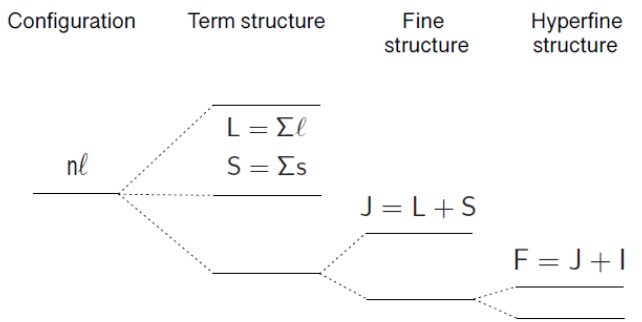


**Figure 1:** Schematic energy level splitting for an  $nl$  configuration [3].

#### 2.1.2 The HI 21cm

The ground level of the hydrogen atom is split into two *hyperfine* levels due to the interaction of the angular momenta of the electron and proton (spins). In the case of the hydrogen atom, the total angular momentum can take the values  $F = 0$  (antiparallel case, singlet state) and  $F = 1$  (parallel case, triplet state), as represented in figure 2. The energy difference between the hyperfine levels is [3]

$$\Delta E = \frac{4 g \hbar^4}{3 m_p m_e^2 c^2 a^4} = 5.88 \times 10^{-6} \text{ eV}. \quad (2)$$

The frequency of the photon emitted in the transition from the triplet to the singlet state is

$$\nu = \frac{\Delta E}{h} = 1420 \text{ MHz} \quad (3)$$

or equivalently the wavelength is

$$\lambda = \frac{c}{\nu} = 21 \text{ cm}. \quad (4)$$

The transition that produces this line is highly forbidden and requires an extremely rarefied gas: in a single hydrogen atom it occurs approximately once every  $10^7$  years [3]. However, the enormous amount of hydrogen in the spiral arms of the Milky Way makes the radiation observable at any given time and can be easily detected by radio telescopes.

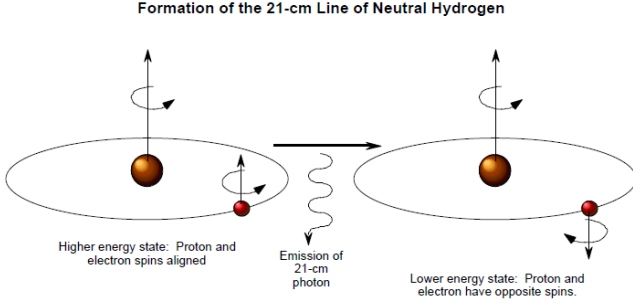


**Figure 2:** Interaction between the electron and proton spins in the hydrogen atom.

## 2.2 Doppler Effect

Due to the relative motion between the source and the observer, the observed frequencies of emission lines are shifted by the Doppler effect. In terms of the wavelengths we have

$$\frac{\lambda_{oss} - \lambda_{lab}}{\lambda_{lab}} \approx \frac{v}{c} \quad (5)$$

where  $c$  indicates the speed of light in a vacuum,  $v$  is the relative velocity,  $\lambda_{lab}$  is the wavelength at which a certain line is observed from a frame of reference comoving with the system that emitted such line (the so called *laboratory frame*), while  $\lambda_{oss}$  refers to the wavelength at which the line is actually observed as a consequence of a Doppler shift. Equation 5 is valid for non-relativistic speeds. In our case, we expect velocities of the order  $V_r \sim 10^2 \text{ km/s}$  so it is a valid approximation.

## 2.3 The rotation curve of the Milky Way

The emission line of HI can be used to study the velocity of neutral hydrogen clouds thanks to the Doppler effect formula in Eq. 5. Measuring the shift in wavelength  $\lambda_{oss}$  with respect to the known value  $\lambda_{lab}$  measured in the rest frame, it is thus possible to determine the relative velocity  $V_r$  between the cloud and the observer along the line of sight (*l.o.s.*). In this report we will assume that all the constituents of the Galactic disk move approximately along circular orbits in the galactic plane with uniform speed. We now define  $R_0$  and  $V_0$  as the radius between the observer (the Sun) and the Galactic center (*GC*) and the tangential velocity of the Sun respectively. We adopt the values  $R_0 = 8.5 \text{ kpc}$  and  $V_0 = 220 \text{ km/s}$ .

We are interested in studying the rotation curve  $V(R)$  of the Milky Way, which describes the rotational speed of the Galaxy at different distances from the *GC*. We consider a cloud  $M$  moving at speed  $V$  along a circular orbit of radius  $R$ . The cloud has galactic longitude  $l$  and  $r$  indicates its distance from the Sun. A schematic representation is shown in Fig. 3. After a simple geometric procedure, it is possible to write the relative velocity  $V_r$  along the line of sight, between us and the cloud, as

$$V_r = V \frac{R_0}{R} \sin(l) - V_0 \sin(l). \quad (6)$$

This equation is valid for all longitudes  $l$ . However, measuring  $V_r$  alone for any given  $l$  is not enough to solve this equation to derive both  $V$  and  $R$  (the problem is underdetermined). To address this problem, we restrict the analysis to the first quadrant only. When observing in any given direction, we will measure the emission coming from multiple clouds along the *l.o.s.* at once, resulting in multiple components in the observed spectrum. Assuming Keplerian motion, clouds located farther from the Galactic center will move at velocities equal to or lower than those of clouds closer to the center. In this case, the highest measured radial velocity  $V_{r,max}$  originates from the cloud located at the tangent point  $\mathbf{T}$  (Fig. 3), since the maximum possible projected velocity occurs when the projection angle is zero. Observing quadrant I only, this point is uniquely determined. For a cloud at the tangent point we see from Fig. 3 that the cloud location is given by

$$R = R_0 \sin l. \quad (7)$$

This simplifies equation 6 so that, at the tangential point, we have

$$V = V_{r,max} + V_0 \sin l. \quad (8)$$

It is now possible to use equations 7 and 8 to calculate the rotation curve  $V(R)$  by measuring  $V_{r,max}$  at different  $l$  in the first quadrant. It is reasonable to assume the measured rotation curve to be valid also in the other three quadrants by symmetries.

It is important to note that the *tangent-point method* may be affected by systematic errors. When material located along the *l.o.s.* (not necessarily confined to the galactic disk) follows orbits with rotational velocities significantly higher than those at the tangent point, the *l.o.s.* component of their velocity can exceed that of the material on the tangent orbit. As a result, the observed maximum Doppler shift may originate from regions other than the tangent point, introducing systematic errors into the measurements.

## 2.4 Mapping The Milky Way

In order to map the Milky Way, it is necessary to determine the position of the detected HI clouds. To do so, we use all the velocity components observed in the spectra (not just the maximum ones as in the previous section). Moreover, we are interested in mapping all observable directions, not just quadrant I.

We assume that the gas in the Milky Way is characterized by *differential rotation*, meaning that the Milky Way does not rotate like a rigid body and therefore the angular velocity depends on the distance from the Galactic center. We then assume that all velocities are constant

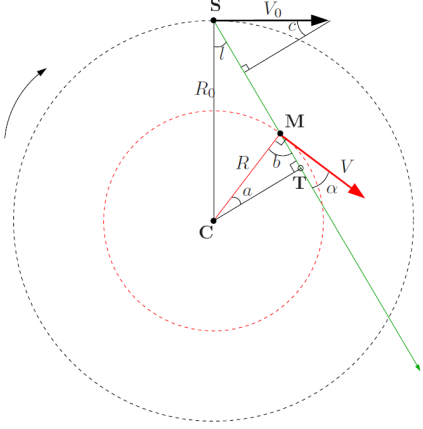


**Figure 3:** Geometry of the Galaxy. **C** is the location of the Galactic center, **S** that of the Sun, **M** that of a gas cloud that we want to observe. The SM line is the line-of-sight. The arrow on an arc indicates the direction of rotation of the Galaxy. The arrows on line segments indicate the velocity of the Sun ( $V_0$ ) and the gas cloud ( $V$ ). [5]

and equal to that of the Sun  $V(R) = V_0 = \text{constant}$ , as most of the spiral galaxies exhibit flat rotational curves which indicate that  $V(R)$  does not depend upon  $R$  after a certain point. We will check the consistency of this assumption once we have plotted the rotation curve of the galaxy. Equation 6 then simplifies to

$$V_r = V_0 \sin \left( \frac{R_0}{R} - 1 \right), \quad (9)$$

and so

$$R = \frac{R_0 V_0 \sin l}{V_0 \sin l + V_r}. \quad (10)$$

From the measurement of  $V_r$ , since  $l$ ,  $R_0$  and  $V_0$  are known, using Eq. 10 it is possible to determine the distance  $R$  of the cloud from the Galactic center. It should be noted that if the observation is made in quadrants II and III, the position of the emitting gas clouds can be uniquely determined. However, if the observation is made in quadrants I and IV, there may be two possible positions corresponding to a given  $l$  and  $R$ : one closer to us than the tangent point **T** (the cloud at point **M** in Fig. 3), and one farther away, at the intersection of line **ST** with the inner circle (see Fig. 3).

By applying the *law of cosines* in triangle **CSM**, we can calculate the distance  $r$  of the cloud from the Sun

$$r_{\pm} = \pm \sqrt{R^2 - R_0^2 \sin^2 l + R_0 \cos l}. \quad (11)$$

Equation 11 is a second-order equation and provides two possible values of  $r$ . The negative solutions has no physical meaning (it would imply that the cloud is located on the opposite side of the Galactic Center with respect to the Sun) and must therefore be discarded. In quadrants II and III,  $R$  is always greater than  $R_0$  and  $\cos l < 0$ , which means that there is one and only one positive solution  $r_+$ . In quadrants I and IV, two positive solutions may exist, both of which are physically plausible. In such cases, it is not possible to determine the correct one without additional observations. To resolve this ambiguity, we reobserve in the same Galactic longitude but at a small non-zero Galactic latitude. If the ambiguous cloud is distant, it should no longer be visible. If it is nearby, it should still be detectable even when observing slightly off the plane.

In this way, the ambiguity should be resolved; otherwise, it is not possible to discriminate the correct value.

From the values of  $r$  obtained by Equation 11 we can convert to Cartesian coordinates

$$\begin{cases} x = r \cos(l - 90^\circ), \\ y = r \sin(l - 90^\circ). \end{cases} \quad (12)$$

By computing the values of  $x$  and  $y$  for different velocities at various longitudes, we can plot these points on a graph to visualize the structure of the Galaxy and map the Milky Way. Note that this will show the map with the Sun in the center, at position  $(0, 0)$ . In order to plot the map with the Galactic center at  $(0, 0)$ , it's necessary to add  $R_0$  to the  $y$ -coordinate of each point

$$\begin{cases} x = r \cos(l - 90^\circ), \\ y = r \sin(l - 90^\circ) + R_0. \end{cases} \quad (13)$$

### 3 SALSA Radio Telescope

SALSA-Onsala (*Such A Lovely Small Antenna*) is a radio telescope located at the Onsala Space Observatory in Sweden ( $12^\circ 01' 00''$  E,  $57^\circ 25' 00''$  N), designed to introduce students to radio astronomy. There are three SALSA telescopes available (Brage, Vale, and Torre, Fig. 4), all with the same specifications (see Tab. 1), and can be controlled remotely through the Internet connecting to the site <http://vale.oso.chalmers.se/salsa>. Each radio telescope has an antenna with a diameter of 2.3 m, which corresponds to an angular resolution of  $7^\circ$  at the HI line frequency (1420 MHz). Indeed, radio telescopes are diffraction-limited instruments, and their angular resolution is constrained by the size of the *diffraction pattern* (or *Airy disk*), whose characteristic size is given by

$$\alpha_A = 1.22 \frac{\lambda}{D} \quad [\text{rad}] \quad (14)$$

where  $\lambda$  is the wavelength of the radiation and  $D$  is the (circular) aperture of the telescope.

The telescope is designed to operate at 1420 MHz, and it is composed of several main components:

- a 2.3 m satellite dish on a fully steerable, motorized azimuth-elevation mount;
- a rotor controller to run the motors which steer the telescope. It allows to track objects with an accuracy of  $0.125^\circ$  in perfect conditions. However, if it is windy the telescope may wobble in the wind (around the wanted position) and hence disturb the pointing of the telescope during small time intervals with  $1-2^\circ$ ;
- a feed composed of a helical antenna backed by a cavity;
- a super-heterodyne receiver providing 10 MHz bandwidth centered on the 1420.4 MHz (21-cm) hydrogen line;
- a low-noise amplifier;
- A/D (Analog-to-Digital) converter;

**Table 1:** Technical specifications of SALSA. [14] & [6]

Parameter	Value
Diameter	2.3 m
Focal length	0.9 m ( $f/0.37$ )
Angular resolution	$7^\circ$ at 1420 MHz
Frequency range	$1420 \pm 20$ MHz
Frequency resolution	9.375 kHz (2.4 MHz over 256 frequency channels)
Noise diode temperature	$\approx 100$ K
System temperature	$\approx 500$ K
Aperture efficiency	$\approx 50\%$
Mount	two-axis azimuth/elevation
Pointing accuracy	$\approx 0.125^\circ$
Travel limits	0–90° vertically, 0–360° horizontally

- software (named *qradio*) on a desktop computer to receive and process data from the telescope and control it.

More details of the instruments can be found in [6].



**Figure 4:** SALSA radio telescopes.

### 3.1 Limitations

Although the small size of the SALSA telescope limits both its sensitivity and angular resolution, it is equipped with a strong and sensitive receiver that enables the detection of emissions from HI clouds. However, it is not capable of detecting the weaker HI signals originating from lower-density regions.

While the telescope is technically capable of observing down to the horizon, it is advisable to restrict observations to sufficiently high altitudes to avoid contamination from terrestrial radio interference. As a general rule of thumb, the target altitude should be greater than  $15^\circ$ .

## 4 Observation

For this observation, the Torre radio telescope was operated remotely from Pisa. Various regions along the Galactic disk were observed. The observation began on 2024-11-14 at 16:07:41 UTC and ended at 17:52:43 UTC. During this time window, only the regions between  $l = 20^\circ$  and  $l = 170^\circ$  were above  $15^\circ$  in altitude, and therefore only this portion of the Galactic plane could be observed.

To determine which objects were visible during the observation window, a Python script was written to compute the rise and set times of several points at different galactic coordinates. The results were verified using the *Stellarium* software (available at <http://stellarium.org/>).

The Galactic coordinates of the observation's targets are shown in Table 2. For the measurements in quadrant I, we took spectral images at different Galactic latitudes for each longitude in order to resolve the ambiguity discussed in Section 2.4. Due to the limited time available, we were able to take three measurements (at  $b = 0^\circ, 3^\circ$ ,

and  $-3^\circ$ ) for some longitudes and only two (at  $b = 0^\circ$  and  $3^\circ$ ) for others, as presented in Tab. 2.

**Table 2:** Coordinates used in the observation campaign. Each pair of columns indicates a direction ( $l, b$ ) explored.

Quadrant I		Quadrant I		Quadrant II	
$l$ ( $^\circ$ )	$b$ ( $^\circ$ )	$l$ ( $^\circ$ )	$b$ ( $^\circ$ )	$l$ ( $^\circ$ )	$b$ ( $^\circ$ )
20	-3, 0, 3	35	0, 3	110	0
30	-3, 0, 3	45	0, 3	120	0
40	-3, 0, 3	55	0, 3	130	0
50	-3, 0, 3	65	0, 3	140	0
60	-3, 0, 3			150	0
70	-3, 0, 3			160	0
80	-3, 0, 3			170	0
				180	0

### 4.1 Telescope settings

The telescope was controlled using the *qradio* software. For each measurement, we set the Galactic longitude  $l$  and latitude  $b$ , and the telescope automatically moved to point in the specified direction. Once in position, we enabled the *tracking option*, and the telescope started to follow the target automatically for the duration of the measurement.

To obtain a clearer signal, we chose an integration time of 120 seconds. The telescope automatically divides the specified integration time into two parts. This is because, in addition to observing the target, the telescope must also measure its own system noise (i.e., how the receiver itself affects the detected signal). To achieve this, the telescope shifts the measurement frequency away from the hydrogen line when calibrating its internal noise.

By default, the *qradio* software performs the following tasks:

- **LSR correction:** The frequency shift observed is due to the relative motion between the telescope (observer) and the target (source) along the line of sight. The radial velocity and observed frequency are corrected with respect to the Local Standard of Rest (LSR), taking into account both the Sun's motion relative to the LSR and the Earth's orbital motion around the Sun.
- **RFI removal:** SALSA uses median filtering to suppress any Radio Frequency Interference (RFI) present in the recorded signal. This filter replaces each value in the signal with the median of neighbor-

ing values, helping to identify and remove spurious peaks due to interference (see Fig. 5).

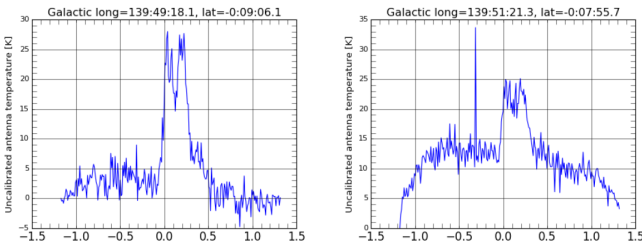


**Figure 5:** Example of RFI removal in SALSA. The spectrum on the left side was obtained with default settings where RFI is filtered away. The other spectrum is a result of a subsequent measurement where the RFI removal option was disabled. One can identify a narrow and strong peak that is a result of a disturbance generated by an external radio source [6].

## 4.2 Measurement results

After each measurement, the software provides a FITS file and a TXT file containing the results. We chose to work with the TXT files, as they are easier to read. Each file contains two columns: the first lists the velocities, while the second contains the uncalibrated antenna temperatures.

The uncalibrated antenna temperature  $T$  refers to the intensity of the radiation at a given wavelength  $\lambda$ . The software automatically converts frequencies into radial velocities  $V_r$  along the *l.o.s.* using the Doppler shift formula (see Eq. 5), relative to the 21-cm line of neutral hydrogen (HI). We considered a relative uncertainty of 20% on the measured values of  $T$ . An example of a raw spectrum is shown in Fig. 6.

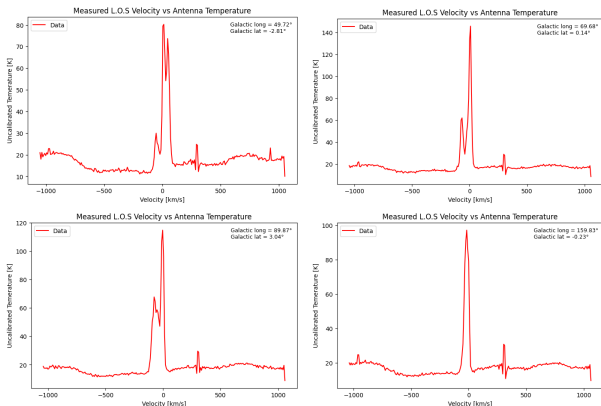


**Figure 6:** Examples of a raw spectra taken with SALSA. We can see we have a systematic error.

## 5 Data Reduction and Results

The main steps for data reduction are as follows:

1. Read the data from the Torre telescope.
2. Fit the background noise in order to smooth the data.
3. Identify the peaks in the noise-subtracted data to obtain the corresponding radial velocities .

4. Fit gaussian functions to the peaks in order to obtain the amplitude and the standard deviation for each peak.
5. To ensure no peak is missing, subtract each curve to the data and perform another gaussian fit on the residuals <sup>1</sup>.
6. Convert the obtained peaks to radial velocities in the LSR.
7. Find the position of the detected HI cloud in the Milky Way and plot rotation curves with spiral arm diagrams.
8. Conduct error analysis.

### 5.1 Noise subtraction

While working on data reduction, our first goal was to fit Gaussian curves to each individual spectral line after having isolated and subtracted the noise component. In our case, the parameter  $\mu$  in the Gaussian function

$$G(x) = a \exp\left(\frac{(x - \mu)^2}{2\sigma^2}\right) \quad (15)$$

corresponds to the  $V_r$  of the gas cloud that emitted such line. The analysis described in the following sections was implemented with a Python script.

Notice that in Fig. 6 one can easily see how all the prominent 21 cm lines are concentrated near the value  $V_r = 0$ , as expected (this happens for every data set available, see App. D). This implies that for high values of  $|V_r|$ , the signal is essentially dominated by noise.

Moreover, a peak that is obviously not due to any galactic emission but rather to an instrumental error, appears in many spectra (Fig. 6 and App. D) for  $200 \text{ km/h} \lesssim V_r \lesssim 400 \text{ km/h}$ . For this reason we proceeded to discard the values in said range of  $V_r$ .

A quadratic polynomial function was then fitted to the points with  $|V_r| > 500 \text{ km/s}$  in order to obtain the noise distribution. After subtracting it from the original signal and having discarded the points in the "tail" of the spectra ( $|V_r| > 800 \text{ km/s}$ ) to obtain a better fit for the Gaussian functions afterwards, we were left with a series of data sets similar to the one shown in Fig. 7.

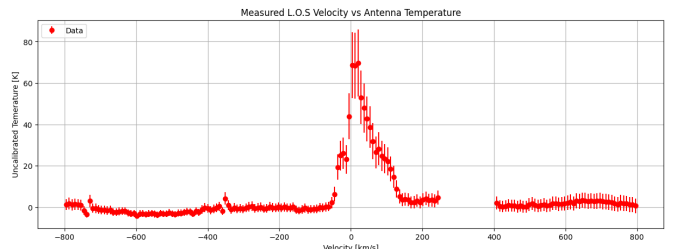


**Figure 7:** Noise-subtracted spectral image of one of the data-frames.

### 5.2 Gaussian fit

A number of Gaussian curves equal to the number of peaks found in each spectral image was fitted. However,

<sup>1</sup>It is possible to iterate this procedure in order to enhance accuracy, although this wasn't necessary in our case.

two emission lines could have originated from HI clouds with very similar values of  $V_r$ , so that the peak of one the clouds might not be detected by the algorithm, appearing only as a small "bump" in the wings of a more prominent line.

To address this issue, additional Gaussian curves were also fitted to the residuals of the initial fit. The parameters obtained from these preliminary operations were then used as starting values for a final global gaussian fit.

The results of this procedure are shown in Fig. 8 (which displays the fitted function, the residuals, and the individual Gaussian components), and in App. D.

For each spectrum, we saved the fitting parameters. The value of  $\mu$  corresponds to the radial velocity  $V_r$  of the detected cloud, and we associated the corresponding  $\sigma$  (the width of the spectral line) as its uncertainty. These results will be used to derive the rotation curve and map the Milky Way in the following sections.

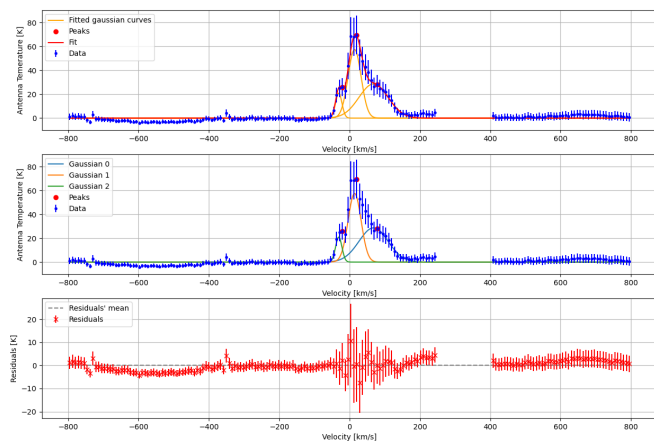


**Figure 8:** At the top: Curve fit of one of the noise-subtracted data frames (with error bars). In the center: Plot of the gaussian curves fitted on each peak (with error bars). At the bottom: Residuals of the fit (with error bars).

### 5.3 Rotation curve

Using the velocities obtained from the fit, as discussed in the previous section, we derived the rotation curve of the Milky Way. As explained in Sec. 2.3, we considered measurements only from quadrant I and, for each spectrum, selected the maximum velocity  $V_{r,max}$  along with its associated uncertainty. We included only measurements taken at  $b = 0^\circ$ , since we are interested in observing the galactic disk where the tangential point  $T$  can be uniquely determined. For each radial velocity, we calculated the corresponding distance  $R$  of the cloud from the GC using Equation 7 and the tangential velocity  $V$  through Eq. 8, along with the associated uncertainties derived via error propagation. For the error in longitude, we adopted the telescope's pointing accuracy in presence of wind (see Sec. 3). The results are reported in Tab. 3. Finally, we plotted the velocity as a function of radius, producing the graph shown in Fig. 9a.

### 5.4 Map of the Milky Way

To create a map of the Milky Way, we used all the HI clouds detected in each spectrum, along with their corresponding velocities measured along the *l.o.s.*, as described

in Sec. 2.4. To each detection, we associated an uncertainty represented by the  $\sigma$  parameter obtained from the gaussian fit, as previously discussed. We then calculated the radius  $R$  from the GC using Eq. 10 and the distance  $r$  from the Sun using Eq. 11. All uncertainties were derived via standard error propagation. We discarded all negative values of  $r$ , as they are unphysical. In cases of multiple positive solutions in quadrant I, we referred to observations at different latitudes  $b$  to resolve the ambiguity. However, for certain clouds this ambiguity could not be resolved, and these cases were excluded from the final dataset. The resulting values are reported in Tab. 5 and 4.

Next, we converted all positions into Cartesian coordinates using Eq. 13, and propagated the associated uncertainties. Finally, we plotted the positions of the HI clouds in a Cartesian reference frame centered at the Galactic Center, obtaining a map of the Milky Way, as shown in Fig. 10a.

## 6 Discussion

The rotation curve obtained in Fig. 9a exhibits the typical behavior known for spiral galaxies. It shows an initial rising trend, followed by a plateau at values around 210 km/s, as expected. This behavior is consistent with rotation curves reported in the literature (such as the one shown in Fig. 9b) and with theoretical models that describe the dynamics of spiral galaxies.

The observed flattening of the rotation curve at large radii  $R$  supports the assumption of a constant tangential velocity  $V(R) = V_0 = \text{const.}$ , made in Sec. 2.3. Moreover, this behavior provides evidence for the presence of a dark matter halo surrounding the galaxy, as discussed in Appendix C.

We also obtained a good map of the Milky Way, highlighting its spiral structure. Thanks to the measurements at different Galactic latitudes  $b$ , we were able to distinguish and identify 118 HI clouds and determine their locations within the Galaxy, as discussed in Sec. 2.4 and 5.4. By comparing Fig. 10a with Fig. 10b, we were able to detect one of the two main arms of the Galaxy, the Perseus Arm. Additionally, we identified two other structures: the Orion Spur, where the Sun is located, and the Outer Arm. We were unable to map the Scutum-Centaurus Arm or other structures, as our observations were limited to Galactic longitudes between  $20^\circ$  and  $170^\circ$ .

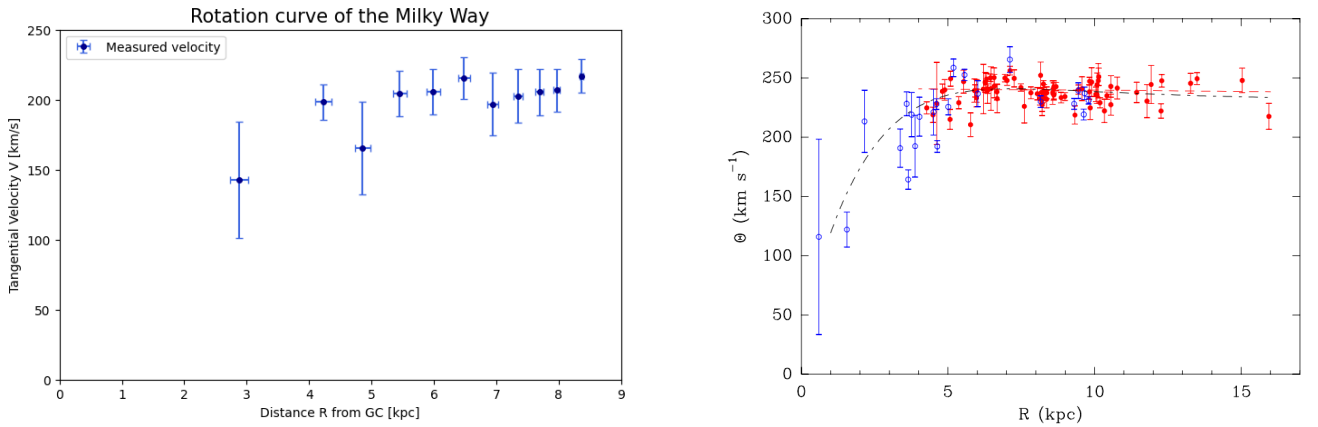
Considering the small size of the Torre telescope compared to large professional radio telescopes, the errors in both the rotation curve and the Milky Way map are well within acceptable limits for our purposes.

## 7 Conclusion

The Milky Way's rotation curve and arms were successfully mapped using HI clouds. Thanks to spectral observations performed using the Torre telescope, we were able to infer the Doppler shift of the 21 cm lines emitted by those clouds, and therefore their velocities. Finally, through some assumptions about the dynamics of the galaxy, the distance of the clouds from the Milky Way's center was evaluated. Error analysis was performed on the computed quantities.

**Table 3:** The table reports the maximum line-of-sight velocities  $V_{r,max}$  measured in the first Galactic quadrant with their associated errors. The tangential velocities  $V$  and distances  $R$  from the Galactic center calculated for each cloud, along with their respective uncertainties, are also reported.

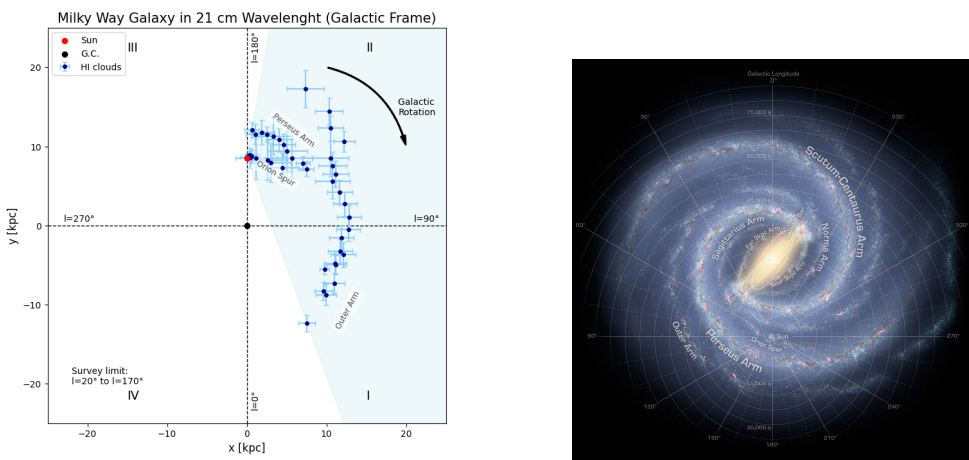
$l$ ( $^{\circ}$ )	$V_{r,max}$ (km/s)	$V_{r,max}$ (km/s)	$V$ (km/s)	$V$ Errors	$R$ (kpc)	$R$ Errors (kpc)
19.81	68.09	41.46	142.63	41.61	2.88	0.14
29.86	88.79	12.04	198.33	12.49	4.23	0.13
34.84	39.73	33.15	165.42	33.31	4.86	0.12
39.92	63.25	15.74	204.44	16.01	5.46	0.11
44.8	50.63	16.08	205.66	16.31	5.99	0.11
49.71	47.59	14.51	215.41	14.73	6.48	0.12
54.77	16.92	22.33	196.63	22.44	6.94	0.09
59.94	12.36	18.85	202.63	18.95	7.35	0.07
64.85	6.29	16.37	205.44	16.45	7.69	0.06
69.68	0.47	15.12	206.79	15.26	7.97	0.05
79.83	0.33	11.98	216.88	11.99	8.37	0.03



(a) Rotation curve of the Milky Way. The tangential velocities  $V$  are shown along with their respective error bars. We observe the typical flattened trend characteristic of the rotation curves of spiral galaxies.

(b) Rotation curve of the Milky Way obtained by the study of parallax and proper motions in [13]. In this paper the Sun position is  $R_0 = 8.34 \pm 0.16$  kpc and its velocity is  $V_0 = 240 \pm 8$  km/s.

**Figure 9:** Comparison of two rotation curves of the Milky Way.



(a) Map of the Milky Way obtained by observing HI clouds in the Galactic disk. The frame is centered on the Galactic Center, with the Sun marked as a red dot. Blue dots, along with their corresponding error bars, represent the positions of the clouds. The survey spans Galactic longitudes from  $20^{\circ}$  to  $170^{\circ}$ . Three spiral arms of the Milky Way are distinguishable: Orion Spur, Perseus Arm and the Outer Arm.

(b) Structure of the Milky Way. We can see two major arms (Scutum-Centaurus and Perseus) and two minor arms (Norma and Sagittarius) located between the major arms. The major arms consist of the highest densities of both young and old stars; the minor arms are primarily filled with gas and pockets of star-forming activity. The Sun lies near a small, partial arm called the Orion Arm, or Orion Spur, located between the Sagittarius and Perseus arms. [Credit: NASA/JPL-Caltech/R. Hurt (SSC/Caltech)]

**Figure 10:** Comparison of our maps (left) and the Nasa's map (right) of the Milky Way.

## A Galactic Coordinates

This is a coordinate system completely independent of the Earth and centered on our Galaxy. The fundamental plane is the *Galactic Plane*, which is where most stars are concentrated. It intersects the celestial sphere along the band of the Milky Way.

The galactic coordinates are:

- **Galactic Latitude ( $b$ ):** it is measured in degrees from  $0^\circ$  to  $\pm 90^\circ$ , perpendicular to the galactic plane.  $b = 0^\circ$  corresponds to the Galactic plane,  $b = 90^\circ$  to the so called the North Galactic Pole;
- **Galactic Longitude ( $l$ ):** it is measured in degrees from  $0^\circ$  to  $360^\circ$ , *counterclockwise*, starting from the direction of the Galactic Center.

The origin of the reference system is conventionally chosen to point toward the Galactic Center (GC). The Galaxy is divided into four quadrants, labeled by Roman numbers:

- Quadrant I,  $0^\circ < l < 90^\circ$ ;
- Quadrant II,  $90^\circ < l < 180^\circ$ ;
- Quadrant III,  $180^\circ < l < 270^\circ$ ;
- Quadrant IV,  $270^\circ < l < 360^\circ$ .

In Quadrants I and IV we observe mainly the inner part of our Galaxy. Quadrants II and III contain material lying at galacto-centric radii which are always larger than the Solar radius.

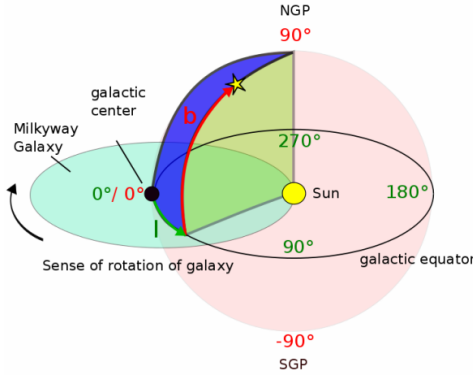


**Figure 11:** Illustration of the Galactic coordinate system, with longitude ( $l$ ) and latitude ( $b$ ).

## B Local Standard of Rest

The *Local Standard of Rest* (LSR) is a reference frame associated with the average motion of matter in the Milky Way in the vicinity of the Sun. Let us assume that:

1. The mass distribution of our Galaxy is approximately axisymmetric, so that the gravitational force acting on a mass located in the galactic plane is always directed toward the Galactic Center.
2. The Galaxy is in a steady state, meaning that the acting forces are time-independent (or vary so slowly that their evolution can be neglected).

Under these assumptions, for every point in the galactic plane, there exists a velocity  $(\Pi, \Theta, Z)_{LSR} = (0, \Theta_0, 0)$ , with  $\Theta_0 = \text{const.}$ , such that an object located at that point will move in uniform circular motion around the Galactic Center, with a trajectory confined to the galactic plane. Any such point can be used as a reference frame in velocity space and is called the *Local Standard of Rest* (Fig. 12), with  $\Theta_0(R)$  being the constant *circular velocity* that depends on the position  $R$  with respect to the Galactic Center.

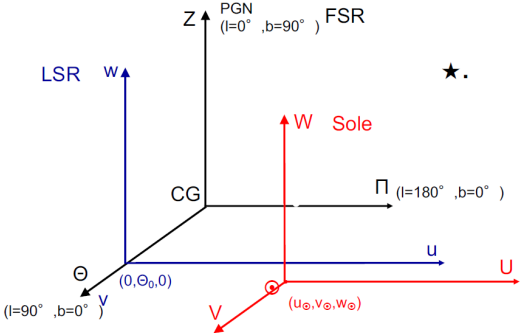


**Figure 12:** Local Standard of Rest, in blue. In red is shown the reference frame attached to the point representing the Sun in velocity space (note that it is not centered on the real Sun, whose components vary over time), while the black star represents a generic star in the Galaxy. [7]

The Sun is not a *Local Standard of Rest* object, since it does not rotate in uniform circular motion, although it is very close to the *circular velocity*  $\Theta(R_\odot) = V_0$  corresponding to its distance from the Galactic Center.

## C Keplerian Motion and Dark Matter

A theoretical model to describe the rotation curve of a galaxy can be derived from Newtonian physics. We assume that the various components making up the galaxy move in uniform circular motion along circular orbits around the galactic center. The centrifugal acceleration due to circular motion is balanced by the gravitational acceleration and so we obtain the following relation

$$V_{\text{Keplerian}}(R) = \sqrt{\frac{GM(R)}{R}}. \quad (16)$$

where, according to the shell theorem,  $M(R)$  is the mass enclosed within the radius  $R$  respect the Galactic center. This rotation curve is called *Keplerian*.

The majority of a galaxy's mass is in the form of stars. By studying the galaxy's luminosity, we can estimate its mass using stellar physics. Astronomical observations show that most of the visible mass is concentrated towards the center (usually within the first 10 kpc) and decreases rapidly in the outer regions. Therefore, one would expect a rotation curve that increases in the inner regions, where the mass is concentrated, and then decreases in the outer parts (see Fig. 13).

Surprisingly, this is strongly at odds with observations. The rotation curves measured from kinematic studies (i.e., those probing the galaxy's gravitational properties, accounting for both visible and non-visible matter) display a rising section followed by a flat portion, as shown

in Fig. 13. Assuming the validity of Newtonian physics<sup>2</sup>, one possible explanation for this discrepancy between theory and observation is the existence of a spherical, non-visible component (a dark halo) in which the galaxy is embedded. In this case, the total mass continues to increase even in the outer regions, and with a suitable mass distribution, the rotation curve flattens at large radii. A possible constituent of this halo is dark matter.

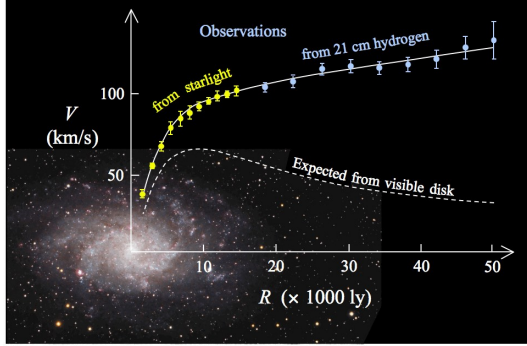


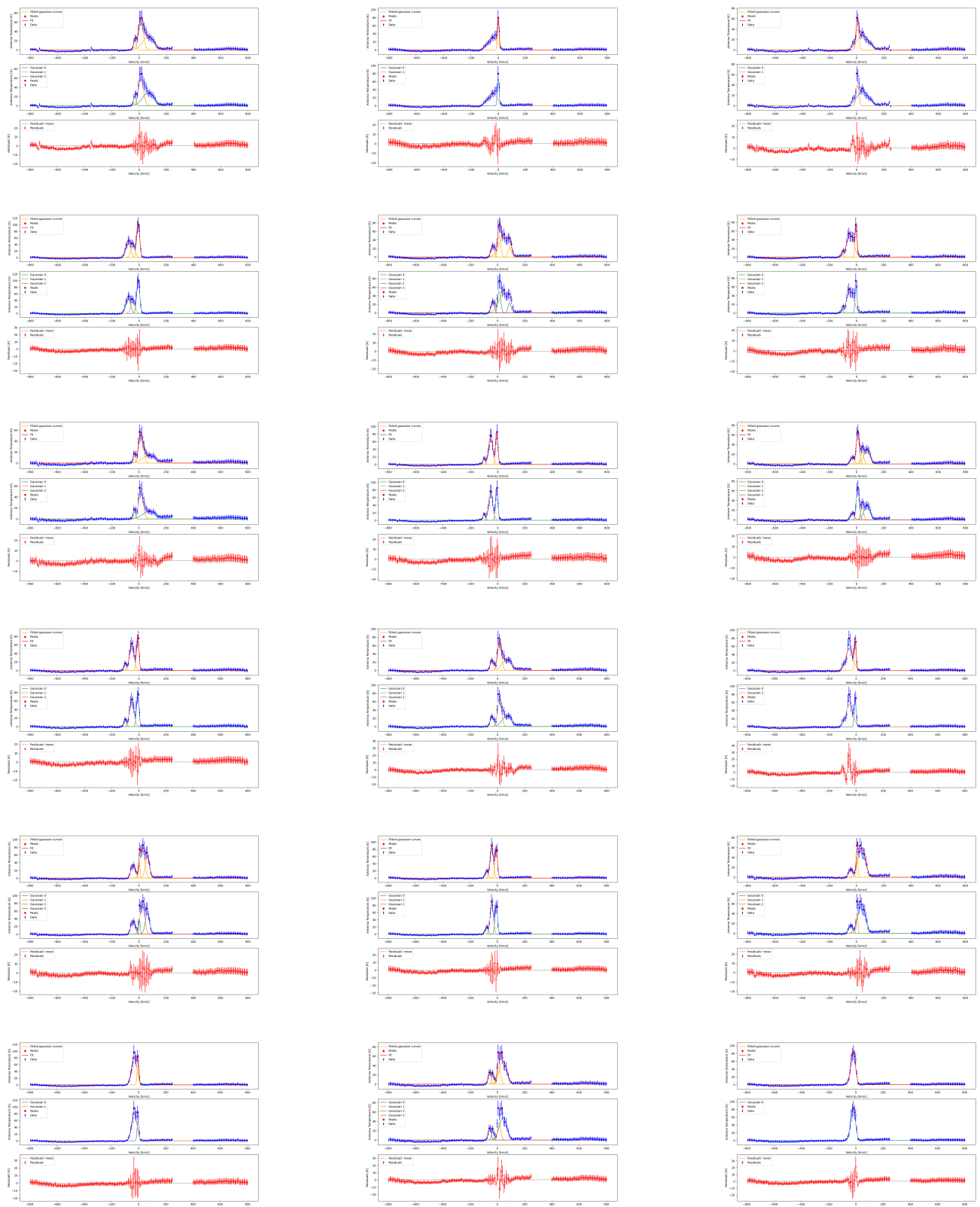
**Figure 13:** Rotation curve of spiral galaxy Messier 33 (yellow and blue points with error bars), and predicted curve from visible matter (gray line). [1]

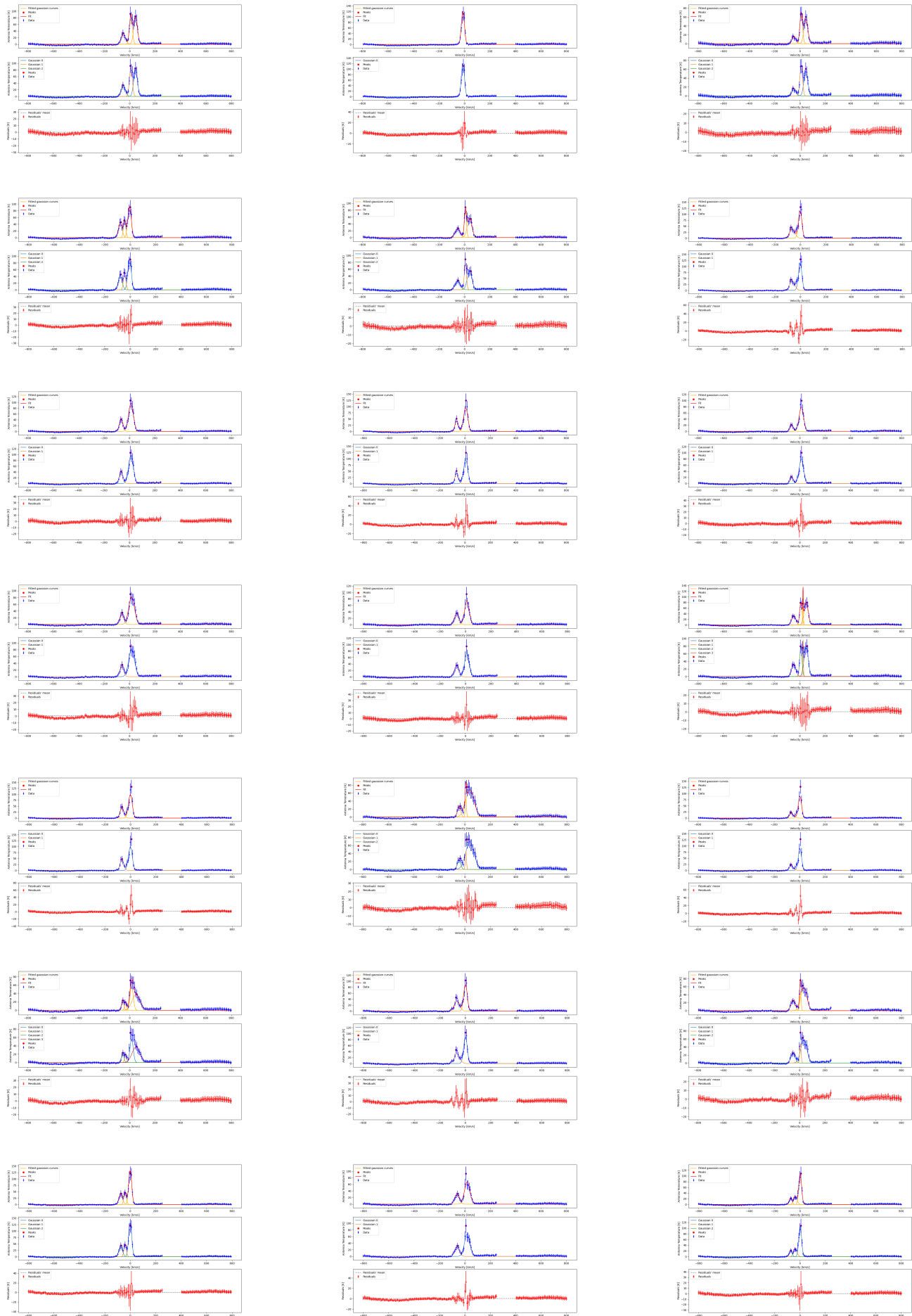
---

<sup>2</sup>To solve this issue, alternative theories such as *MOND* (*M*odified *N*ewtonian *D*ynamics) have been proposed. These attempt to explain the observed spiral galaxy rotation curves without invoking dark matter by modifying Newtonian dynamics at low accelerations.

## D Data reduction results

All the spectral images obtained at the end of the data reduction process are shown below.





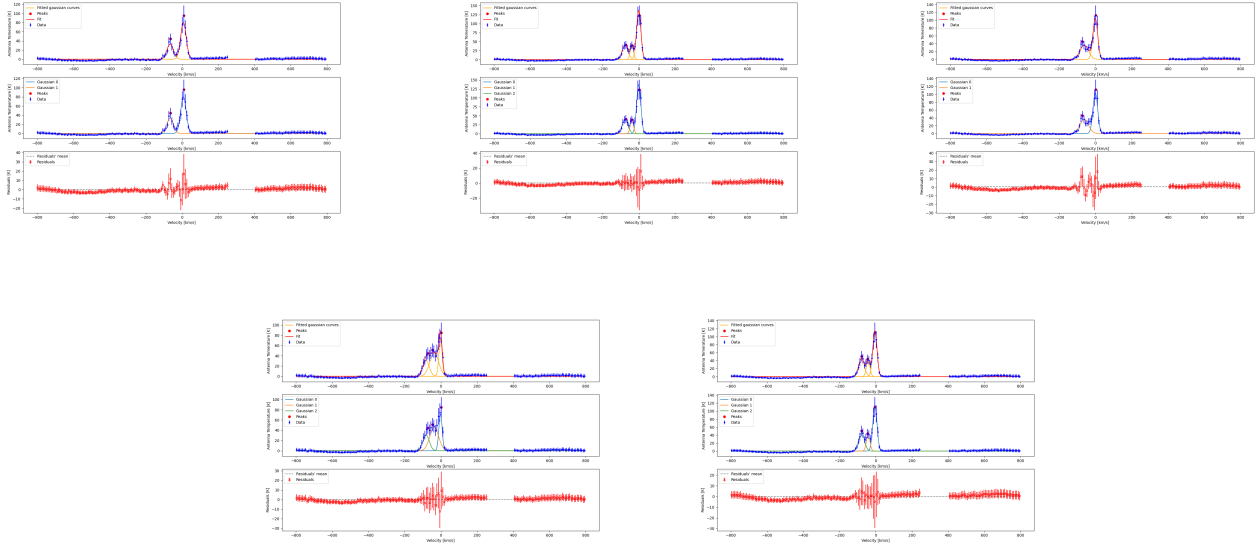


**Figure 14:** For each image: *At the top*: Curve fit of one of the noise-subtracted data frames (with error bars). *In the center*: Plot of the gaussian curves fitted on each peak (with error bars). *At the bottom*: Residuals of the fit (with error bars).

## E Tabulars

**Table 4:** The table reports the galactic coordinates, tangential velocities  $V$ , distances  $R$  from the *Galactic Center* (GC), and the distances from the Sun of the detected neutral hydrogen clouds whose positions could be determined. Each measurement is associated with its respective uncertainty. The seventh and eighth columns show the results obtained from Eq. 11. We can observe that, for measurements in quadrant II, only one of the two solutions is physically meaningful (the other being negative). For measurements in quadrant I, however, the ambiguities discussed in Sec. 2.4 arise. For the clouds listed, the observations at different galactic latitudes  $b$  allowed us to resolve this ambiguity.

$l$ (°)	$b$ (°)	$V$ (km/s)	$V$ Errors (km/s)	$R$ (kpc)	$R$ Errors (kpc)	$r_1$ (kpc)	$r_2$ (kpc)	$r$ (kpc)	$r$ Errors (kpc)
79.83	-2.87	-35.95	13.98	10.19	0.79	7.32	-4.32	7.32	1.39
79.83	-2.87	2.22	11.07	8.41	0.43	2.39	0.61	2.39	4.02
79.83	-2.87	-74.01	11.6	12.91	1.05	11.34	-8.34	11.34	1.38
79.83	0.16	-74.05	14.04	12.92	1.27	11.34	-8.34	11.34	1.67
79.83	0.16	0.33	11.98	8.49	0.47	2.93	0.08	2.93	2.08
79.83	0.16	-39.27	9.57	10.38	0.56	7.65	-4.65	7.65	0.95
79.85	3.09	-38.27	9.08	10.32	0.53	7.55	-4.55	7.55	0.90
79.85	3.09	-75.61	16.12	13.06	1.49	11.52	-8.53	11.52	1.95
79.85	3.09	-0.43	11.81	8.52	0.47	3.09	-0.09	3.09	2.05
84.71	0.04	-4.13	13.27	8.66	0.53	2.63	-1.06	2.63	2.51
84.71	0.04	-42.66	9.17	10.56	0.55	7.09	-5.52	7.09	0.92
84.71	0.04	-76.88	14.74	13.13	1.36	10.78	-9.21	10.78	1.78
84.8	3.06	-41.67	9.62	10.52	0.57	6.98	-5.44	6.98	0.97
84.8	3.06	-78.01	15.55	13.22	1.45	10.09	-9.36	10.9	1.92
84.8	3.06	-4.44	11.64	8.68	0.47	2.67	-1.13	2.67	2.15
89.79	-3.01	-40.06	32.76	10.39	1.89	6.01	-5.95	6.01	3.29
89.8	0.01	-81.62	17.82	13.51	1.74	10.53	-10.48	10.53	2.24
89.8	0.01	-36.88	24.51	10.21	1.37	5.69	-5.63	5.69	2.47
89.8	0.01	-2.07	9.17	8.58	0.36	1.22	-1.15	1.02	2.64
89.87	3.04	-43.61	15.54	10.6	0.93	6.35	-6.32	6.35	1.56
89.87	3.04	-80.57	17.53	13.41	1.69	10.39	-10.35	10.39	2.18
89.87	3.04	-5.5	10.74	8.72	0.44	1.96	-1.92	1.96	1.97
99.83	-0.02	-103.09	8.05	16.21	1.15	12.43	-15.33	12.43	1.34
99.83	-0.02	-2.05	6.96	8.58	0.28	0.42	-3.32	0.42	1.28
99.83	-0.02	-44.02	26.09	10.67	1.61	5.15	-8.06	5.15	2.06
109.8	-0.07	-5.63	8.53	8.74	0.37	0.64	-6.43	0.64	0.92
109.8	-0.07	-49.87	15.07	11.22	1.07	4.96	-10.72	4.96	1.53
109.8	-0.07	-98.06	10.12	16.15	1.05	11.15	-16.91	11.15	1.73
119.71	-0.11	-7.25	8.81	8.84	0.42	0.64	-9.07	0.64	0.77
119.71	-0.11	-50.78	16.05	11.58	1.32	4.70	-13.13	4.07	1.72
119.71	-0.11	-99.38	9.32	17.71	1.08	11.89	-20.31	11.89	1.98
129.74	-0.17	-5.17	6.78	8.77	0.36	0.41	-11.28	0.41	0.54
129.74	-0.17	-47.15	26.02	11.78	2.51	4.37	-15.24	4.37	3.02
139.85	-0.21	-7.15	8.82	8.95	0.59	0.58	-13.57	0.58	0.74
139.85	-0.21	-39.87	11.56	11.82	1.34	3.98	-16.97	3.98	1.52
139.85	-0.21	-77.58	11.9	18.76	3.49	11.44	-24.44	11.44	3.65
149.75	-0.25	-4.04	6.53	8.82	0.55	0.37	-15.05	0.37	0.63
149.75	-0.25	-31.54	19.00	11.88	2.86	3.74	-18.42	3.74	3.06
159.83	-0.23	-20.24	16.84	11.59	3.59	3.24	-19.19	3.24	3.71
169.68	-0.26	-11.66	12.03	12.07	6.55	3.61	-20.34	3.61	6.06

**Table 5:** The table reports the galactic coordinates, tangential velocities  $V$ , distances  $R$  from the *Galactic Center* (GC), and the distances from the Sun of the detected neutral hydrogen clouds whose positions could be determined. Each measurement is associated with its respective uncertainty. The seventh and eighth columns show the results obtained from Eq. 11. For measurements in quadrant I the ambiguities discussed in Sec. 2.4 arise. For the clouds listed, the observations at different galactic latitudes  $b$  allowed us to resolve this ambiguity.

$l$ (°)	$b$ (°)	$V$ (km/s)	$V$ Errors (km/s)	$R$ (kpc)	$R$ Errors (kpc)	$r_1$ (kpc)	$r_2$ (kpc)	$r$ (kpc)	$r$ Errors (kpc)
19.7	-2.71	46.96	44.58	5.21	1.95	12.35	3.66	12.35	2.33
19.7	-2.71	7.35	10.16	7.73	1.17	15.18	0.82	15.18	1.26
19.8	0.31	68.09	41.46	4.44	1.32	11.38	4.62	11.38	1.73
19.8	0.31	14.19	18.52	7.14	1.64	14.53	1.46	14.53	1.75
19.8	0.31	-30.84	9.08	14.5	3.62	22.21	-6.21	22.21	3.75
20.08	3.31	79.18	50.00	4.15	1.36	10.93	5.03	10.93	1.92
20.08	3.31	15.42	17.10	7.06	1.44	14.41	1.56	14.41	1.58
20.08	3.31	-32.48	8.73	14.91	3.66	22.61	-6.64	22.61	3.74
29.79	-2.71	-30.44	13.62	11.78	2.12	18.37	-3.62	18.37	2.28
29.79	-2.73	10.22	10.59	7.77	0.75	13.9	0.85	13.91	0.90
29.79	-2.72	41.76	10.84	6.15	0.49	11.85	2.91	11.85	0.68
29.79	-2.74	78.27	22.82	4.95	0.62	9.96	4.79	9.96	1.20
29.86	0.28	88.79	12.04	4.69	0.32	9.42	5.34	9.41	0.75
29.86	0.28	13.00	10.87	7.60	0.74	13.68	1.06	13.68	0.89
29.86	0.28	45.92	37.00	5.99	1.44	11.61	3.13	11.61	2.04
29.86	0.28	-36.35	12.26	12.72	2.24	19.37	-4.63	19.37	2.38
29.99	3.28	-39.45	13.17	13.26	2.58	19.92	-5.19	19.92	2.73
29.99	3.28	70.3	35.65	5.18	1.04	10.33	4.39	10.33	1.82
29.99	3.28	15.86	14.49	7.43	0.90	13.46	1.27	13.46	1.13
34.84	0.25	39.73	33.15	6.46	1.31	11.23	2.72	11.23	1.98
34.84	0.25	8.57	4.73	7.96	0.36	13.28	0.67	13.28	0.47
34.84	0.25	-44.94	12.79	13.23	2.16	19.28	-5.33	19.28	2.33
34.84	3.23	-52.99	9.26	14.7	1.98	20.85	-6.89	20.85	2.12
34.84	3.23	16.49	12.95	7.51	0.72	12.71	1.24	12.71	0.94
34.84	3.23	-30.73	8.13	11.25	1.05	17.12	-3.17	17.12	1.16
34.84	3.23	51.00	30.86	6.05	1.07	10.58	3.37	10.58	1.83
39.7	-2.82	38.54	27.05	6.67	1.02	10.41	2.66	10.41	1.76
39.7	-2.82	6.22	5.12	8.14	0.34	12.6	0.48	12.63	0.46
39.7	-2.82	-43.07	13.23	12.26	1.7	17.53	-4.45	17.53	1.93
39.92	0.24	63.25	15.74	5.87	0.47	8.69	4.35	8.69	1.27
39.92	0.24	25.80	17.46	7.19	0.77	11.2	1.84	11.21	1.18
39.92	0.24	5.36	4.93	8.19	0.33	12.63	0.41	12.63	0.45
39.92	0.24	-42.09	15.69	12.11	1.95	17.33	-4.29	17.33	2.18
39.97	3.23	41.67	27.12	6.56	0.98	10.16	2.87	10.16	1.77
39.97	3.23	14.05	11.04	7.73	0.57	11.99	1.04	11.99	0.82
39.97	3.23	-32.53	8.66	11.04	0.93	16.11	-3.08	16.11	1.07
39.97	3.23	-55.63	10.78	14.02	1.82	19.42	-6.4	19.42	1.97
44.8	0.20	8.91	9.12	8.04	0.47	11.39	0.67	11.39	0.71
44.8	0.20	-46.67	16.79	12.16	1.93	16.62	-4.55	16.62	2.19
44.8	0.20	26.2	2.58	7.27	0.16	10.15	1.91	10.15	0.31
44.8	0.20	50.63	16.08	6.41	0.51	8.31	3.76	8.31	1.45
44.82	3.19	7.02	5.43	8.13	0.31	11.53	0.53	11.53	0.47
44.82	3.19	33.88	23.94	6.98	0.89	9.60	2.46	9.60	1.75
44.82	3.19	-50.98	16.18	12.66	1.99	17.19	-5.13	17.19	2.26
49.71	0.17	47.59	14.51	6.62	0.45	6.84	4.15	6.84	2.25
49.71	0.17	10.74	11.3	7.99	0.52	10.16	0.83	10.16	0.89
49.71	0.17	-48.92	16.83	12.00	1.71	15.59	-4.65	15.59	2.03
49.72	-2.81	10.74	10.34	7.99	0.47	10.16	0.83	10.16	0.82
49.72	-2.81	-46.34	16.79	11.74	1.63	15.29	-4.29	15.29	1.96
49.72	-2.81	47.45	15.12	6.63	0.47	6.86	4.13	6.86	2.31
49.94	3.22	-52.51	20.22	12.35	2.16	15.97	-5.03	15.97	2.55
49.94	3.22	7.74	8.37	8.13	0.40	10.34	0.6	10.34	0.68
49.94	3.22	40.96	18.07	6.84	0.60	7.57	3.37	7.57	1.95
54.77	0.22	-59.95	14.53	12.75	1.56	15.6	-5.81	15.06	1.86
54.77	0.22	16.92	22.33	7.77	0.89	8.39	1.42	8.39	1.98
54.79	3.21	-62.34	17.52	13.01	1.95	15.91	-6.1	15.91	2.31
54.79	3.21	18.42	21.21	7.71	0.83	8.25	1.55	8.25	1.91
59.79	-2.81	-63.88	13.07	12.08	1.33	14.76	-6.21	14.76	1.63
59.79	-20.81	13.06	17.57	7.95	0.69	7.33	1.23	7.33	1.81
59.85	3.22	-67.61	17.05	13.19	1.84	15.22	-6.68	15.22	2.22
59.85	3.20	12.66	18.19	7.97	0.72	7.35	1.19	7.35	1.86
59.9	0.20	12.3	18.85	7.98	0.75	7.37	1.15	7.37	1.92
59.9	0.20	-64.79	14.29	12.89	1.47	14.85	-6.32	14.85	1.79
64.85	0.15	-64.97	13.94	12.62	1.31	13.61	-6.39	13.61	1.66
64.85	0.15	6.29	16.37	8.24	0.66	6.56	0.66	6.56	1.85
64.97	3.12	-66.41	17.51	12.75	1.68	13.75	-6.56	13.75	2.11
64.97	3.12	7.12	15.52	8.21	0.62	6.43	0.76	6.43	1.82
69.68	0.14	0.47	15.21	8.48	0.62	5.85	0.06	5.85	1.84
69.68	0.14	-65.01	14.89	12.41	1.31	12.46	-6.56	12.46	1.71
69.81	-2.88	-63.72	17.87	12.29	1.54	12.29	-6.42	12.29	2.03
69.81	-2.88	2.91	13.25	8.38	0.53	5.51	0.36	5.51	1.74
69.86	3.14	-63.72	21.49	12.29	1.85	12.28	-6.42	12.28	2.43
69.86	3.14	2.38	14.03	8.04	0.57	5.56	0.29	5.56	1.81
74.75	0.08	-1.25	13.62	8.55	0.55	4.66	-0.19	4.66	1.96
74.75	0.08	-63.33	20.61	12.11	1.68	11.15	-6.68	11.15	2.28
74.97	3.12	-61.79	23.33	11.99	1.86	10.94	-6.53	10.94	2.55
74.97	3.12	-0.47	13.07	8.52	0.53	4.48	-0.07	4.48	1.97

## References

- [1] URL: [https://upload.wikimedia.org/wikipedia/commons/thumb/c/cd/Rotation\\_curve\\_of\\_spiral\\_galaxy\\_Messier\\_33\\_%28Triangulum%29.png](https://upload.wikimedia.org/wikipedia/commons/thumb/c/cd/Rotation_curve_of_spiral_galaxy_Messier_33_%28Triangulum%29.png/1280px-Rotation_curve_of_spiral_galaxy_Messier_33_%28Triangulum%29.png).
- [2] C. J. Bakker and H. C. van de Hulst. *Radiogolven uit het wereldruim.* 's-Gravenhage: Martinus Nijhoff, 1945.
- [3] Fabio Bresolin. *Astronomical Spectroscopy*. 2022.
- [4] Bernard F. Burke, Francis Graham-Smith, and Peter N. Wilkinson. *An Introduction to Radio Astronomy*. Cambridge University Press, 2019.
- [5] Daniel Johansson Cathy Horellou and Eskil Varenius. *SALSA project documentation: Mapping the Milky Way*. 2015. URL: [https://raw.githubusercontent.com/varenius/salsa/main/Lab\\_instructions/HI/English/SALSA-HI\\_English.pdf](https://raw.githubusercontent.com/varenius/salsa/main/Lab_instructions/HI/English/SALSA-HI_English.pdf).
- [6] Eskil Varenius Cathy Horellou Daniel Johansson and Grzegorz Kłopotek. *SALSA user manual: Telescope control and data analysis*. 2018. URL: [https://raw.githubusercontent.com/varenius/salsa/main/User\\_manual/English/SALSA-USERMANUAL\\_English.pdf](https://raw.githubusercontent.com/varenius/salsa/main/User_manual/English/SALSA-USERMANUAL_English.pdf).
- [7] Enrico Maria Corsini. *Astrofisica 1*. Lectures given in the Bachelor's degree program in Astronomy, University of Padua. 2023.
- [8] H. I. Ewen and E. M. Purcell. "Radiation from galactic hydrogen at 1420 Mc./sec". In: *Nature* 168 (1951), p. 356.
- [9] H. C. van de Hulst, C. A. Muller, and J. H. Oort. "The spiral structure of the outer part of the galactic system derived from the hydrogen emission at 21-cm wavelength". In: *Bulletin of the Astronomical Institutes of the Netherlands* 12 (1954), p. 117.
- [10] K. G. Jansky. "Radio waves from outside the solar system". In: *Nature* 132.3323 (July 1933), p. 66.
- [11] Hong-Yu Li and Jia-Hao Hu. *The Rotation Curve and Spiral Structure of Milky Way from the Hydrogen 21-cm Line Detection with Campus Radio Telescope*. 2024. arXiv: 2404.17893 [astro-ph.GA]. URL: <https://arxiv.org/abs/2404.17893>.
- [12] C. A. Muller and J. H. Oort. "The interstellar hydrogen line at 1420 Mc/s and an estimate of galactic rotation". In: *Nature* 168 (1951), p. 357.
- [13] M. J. Reid et al. "TRIGONOMETRIC PARALLAXES OF HIGH MASS STAR FORMING REGIONS: THE STRUCTURE AND KINEMATICS OF THE MILKY WAY". In: *The Astrophysical Journal* 783.2 (2014). DOI: [10.1088/0004-637X/783/2/130](https://doi.org/10.1088/0004-637X/783/2/130).
- [14] Mir Sakhawat Hossain and Banrupa Mallik. "SALSA is an ICT Based Educational Tool for Astrophysics Students to Study Structure and Dynamics of Milky Way Galaxy". In: *2018 21st International Conference of Computer and Information Technology (ICCIT)*. 2018, pp. 1–6. DOI: [10.1109/ICCITECHN.2018.8631979](https://doi.org/10.1109/ICCITECHN.2018.8631979).